Inorganic Chemistry

pubs.acs.org/IC Article

Molecular Boron-Phosphides: From Stable Monomers to Aromaticity-Tunable Smallest Neutral Metallacycles

Akshara Purushothaman,[#] Hao Liang,[#] Farsana Abdul Salam, Antarik Parashar, Maria Francis, Sudip Pan,* Di Sun,* and Sudipta Roy*

Cite This: https://doi.org/10.1021/acs.inorgchem.6c00722 Read Online

ACCESS | Metrics & More | Article Recommendations | Supporting Information

ABSTRACT: Unlike the conventional polymeric boron-phosphide-based (BP) semiconductors, which exhibit limited reactivity, the neutral monomeric BP motif (**1**) is extremely reactive and nonexistent under ambient conditions. Herein, we depict the ligand-engineering strategies for stabilizing the elusive species **1**, initially by employing stereoelectronically tuned donor-based ligands, followed by their successive incorporation into the smallest metallacycles with induced aromaticity, and hence excellent stability. The electron density distribution and chemical bonding of homo- and heterobileptic ligand-stabilized monomers [(L′)BP(L)] (**2**−**7**) [L′, L = singlet carbenes], and the corresponding neutral 3-membered metal(II)dihalide complexes [BP(MX_2)] (**8**−**9′**) and [((L′)BP(L))(MX_2)] (**10**−**17**) [M = Pd/Pt, X = Cl, Br], are investigated by various quantum chemical methods. The remarkable ligand-switched σ and π aromaticity in the unprecedented mixed d- and p-block planar metallacycles is unambiguously confirmed by $NICS_{zz}$ calculations, ELF, AdNDP, GIMIC, and EDDB analyses.

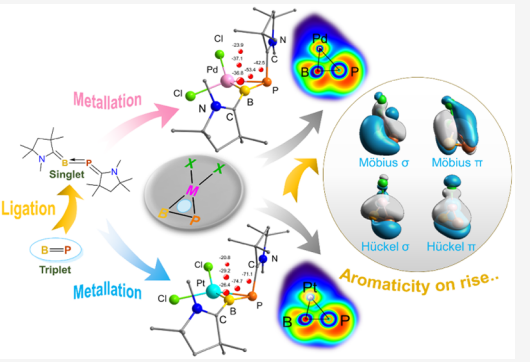

INTRODUCTION

The robust inorganic polymeric material, boron phosphide (BP), has gained significant industrial importance due to its exciting semiconductor and optoelectronic properties. In contrast, the corresponding molecular species have remained elusive under ambient conditions, which could only be identified either in a gaseous state above 900 °C or in a condensed phase at temperatures below 40 K.[1] In 2020, Gilliard and coworkers reported the stabilization of the BP moiety embedded in an aromatic six-membered heterocycle by introducing cyclic alkyl(amino) carbenes (cAACs) via photolysis of the bora-phosphaketene precursor.[2] The aromaticity of the compound was confirmed by nucleus-independent chemical shift (NICS) analysis, exemplifying the first successful incorporation of a highly reactive BP motif into a stable extended π-system, thereby broadening the scope of heteroaromatic chemistry in the stabilization of reactive intermediates. Aromaticity is one of the most intriguing concepts in chemistry, offering deeper insights into the stability and electronic structure of cyclic compounds. Traditionally believed to be an exclusive feature of organic molecules, the experimental observation of MAl_4^- (M = Li, Na, Cu), possessing an all metal aromatic inorganic ring, Al_4^{2-},[3] with a square planar structure and two delocalized π electrons, and thus satisfying the $(4n+2)$ π-electron rule of aromaticity, marked a transformative milestone in broadening the boundaries of chemical bonding and aromaticity. While planar carbocycles and other organocycles stand out through their specific way of overcoming electron deficiency by a non-localizable set of $(4n+2)$ π electrons, all-metal and mixed-main-group element/transition-metal-based aromatic monocycles are scarce in the literature, as metal atoms prefer to form clusters with typical multicentered bonds, narrowing the vivid knowledge of their electronic structures and potential usage as chemical synthons. In 2005, Tsipis et al. reported the presence of all-metal aromaticity in computationally predicted ligand-stabilized cyclic 3-membered Au_3 complexes, relying primarily on the magnetic criterion of the NICS(0) parameter (Figure 1).[4] In 2014, Maestri and coworkers reported the synthesis of the first cationic C_3-symmetric 44-valence-electron triangular Pd_3 cluster, analogous to the cyclopropenyl cation $[C_3H_3]^+$ featuring a delocalized metal−metal bonding framework with a calculated NICS value of −9.7 ppm (Figure 1).[5]

In 2022, Hu and colleagues expanded this field by exploring the aromatic nature of an anionic 4f-metalla-aromatic molecule, PrB_2^- (Figure 1).[6] In 2013, Braunschweig's group reported the stabilization of the first neutral 3-membered metallacycle, comprising a π-diborene and a Pt(0) species (Figure 1).[7] However, to the best of our knowledge, there have

Received: February 6, 2026
Revised: May 11, 2026
Accepted: June 3, 2026

https://doi.org/10.1021/acs.inorgchem.6c00722
Inorg. Chem. XXXX, XXX, XXX−XXX

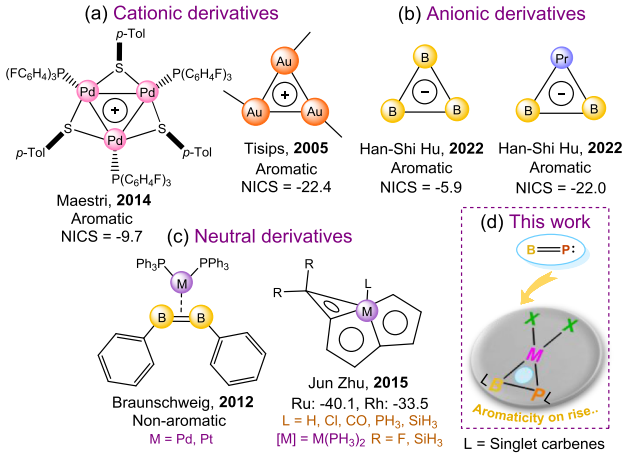

Figure 1. Representative laboratory-isolated and computationally predicted 3-membered metallacycles with cationic (a), anionic (b), and neutral (c) variations. (d) Present work, depicting stabilization of unprecedented mixed d- and p-block neutral planar metallacycles.

been no theoretical or experimental precedents on a monomeric low-coordinate heterodinuclear BP motif incorporated into neutral 3-membered aromatic metallacycles.

Herein, we unravel the stability and chemical bonding of homo- and heterobileptic donor-base-stabilized neutral monomeric two-coordinate boron-phosphides[8] [(L′)B−P(L)] (**2**−**7**): [L′, L = cAAC^{Me} (**2**); L′ = NHC^{Me}, L = cAAC^{Me} (**3**); L′ = cAAC^{Me}, L = NHC^{Me} (**4**); L′, L = NHC^{Me} (**5**); L′, L = acyclic alkyl(amino) carbene (aAAC) (**6**); L′ = 2,4,6-trimethylphenyl (Mes); and L = 2,4,6-tri-isopropylphenyl (Tipp) (**7**)], followed by their subsequent reactivity with metal(II)halides to design the first neutral planar 3-membered cyclic metallaboronphosphide complexes with the general formula [(BP)MX$_2$] (**8**−**9′**) and [((L′)BP(L))(MCl$_2$)] (**10**−**17**) [L′, L = cAAC^{Me}/NHC^{Me}, M = Pd/Pt] (Figure 2). The bonding situation is thoroughly analyzed through the natural bond orbital (NBO), atoms in molecules (AIM), and energy decomposition analysis coupled with natural orbitals for chemical valence (EDA-NOCV) calculations. The unique ligand-switched aromaticity of the predicted metallacycles **8**−**17** was confirmed by the nucleus-independent chemical shift (NICS)[9] calculations, topological analysis of the electron localization function (ELF),[10] adaptive natural density partitioning (AdNDP) analysis, gauge-including magnetically induced currents (GIMIC),[11] and analyses of the electron density of delocalized bonds (EDDB).[12]

COMPUTATIONAL METHODS

Geometry optimizations of monomeric boron-phosphides **2**−**7:** [L′−BP−L] [L′, L = cAAC^{Me} (**2**); L′ = NHC^{Me}, L = cAAC^{Me} (**3**); L′ = cAAC^{Me}, L = NHC^{Me} (**4**); L′, L = NHC^{Me} (**5**); L′, L = aAAC (**6**); L′ = Mes, L = Tipp (**7**)] were performed at the BP86-D3(BJ)/def2-TZVP[13a,b,c] level. The subsequent cyclic metalla-boron-phosphides **8**−**9′** [(BP)MX$_2$] [M = Pd: X= Cl (**8**), Br (**8′**); M = Pt: X = Cl (**9**), Br (**9′**)]; and **10**−**17** [((L′)BP(L))(MCl$_2$)] [L′, L = cAAC^{Me}/NHC^{Me}, M = Pd/Pt] were optimized at the BP86-D3(BJ)/def2-TZVP,[13a,b,c] M06-L/def2-TZVP,[13d] and PBE0-D3(BJ)/def2-TZVP[13e] levels using Gaussian 16.[14] For both M06-L and PBE0 functionals, def2-TZVP was chosen as the basis set for main-group atoms, while def2-TZVP effective core potentials (ECPs) were applied for transition metals (Pd/Pt).[13f] The minima on the potential energy surface were confirmed in each case by the absence of imaginary frequencies. We further conducted CCSD(T) single-point energy

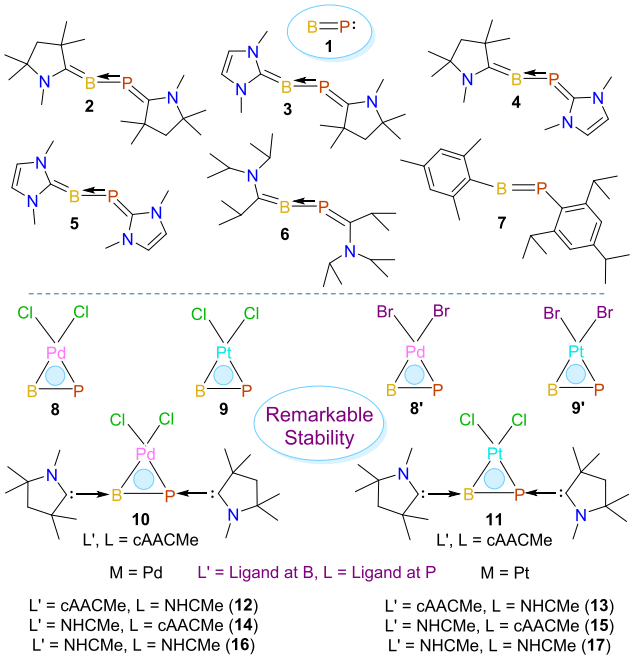

Figure 2. Structures of studied nonligated BP (**1**), ligand-stabilized BP monomers **2**−**7** [(L′)B−P(L)] [L′, L = cAAC^{Me} (**2**); L′ = NHC^{Me}, L = cAAC^{Me} (**3**); L′ = cAAC^{Me}, L = NHC^{Me} (**4**); L′, L = NHC^{Me} (**5**); L′, L = aAAC (**6**); L′ = Mes, L = Tipp (**7**)], and metallacycles **8**−**9′** [(BP)MCl$_2$], **10**−**17** [((L′)BP(L))(MCl$_2$)] [L′, L = cAAC^{Me}/NHC^{Me}]; M = Pd/Pt.

corrections[15] on the M06-L/def2-TZVP optimized geometries (using def2-TZVP for main-group atoms and def2-TZVP ECPs for Pd/Pt, without reoptimization) to refine the relative energy estimations. All DFT calculations were performed with dispersion corrections. To compute Wiberg bond indices (WBI), partial charges (q) on the atoms, and the natural bond orbitals, the NBO 6.0[16a,b] program was used. The ADF 2020.102 software package was utilized to perform the energy decomposition analysis (EDA), coupled with natural orbitals for chemical valence (NOCV). The adaptive natural density partitioning (AdNDP) analyses for **8**−**11** were performed by Multiwfn[11a,b] at the BP86-D3(BJ)/def2-TZVP level. The induced ring current densities of **8**−**11** were calculated at the BP86-D3(BJ)/def2-SVP level using the GIMIC 2.0[17] program. The nucleus-independent chemical shift (NICS) calculations were performed[9] at the M06-L/def2-TZVP level. Topological analysis of the electron localization function (ELF)[10] was done at the BP86-D3(BJ)/def2-TZVP level, and topological analysis of the electron density of delocalized bonds (EDDB)[12] was performed at the M06-L/def2-TZVP level.

RESULTS AND DISCUSSION

Elusive Monomeric BP Species

Optimization of the elusive monomeric BP species **1** in both its singlet and triplet states was carried out at the BP86 and CCSD(T) levels in combination with the def2-TZVPP basis set. The triplet state is 7.6 and 12.3 kcal/mol more stable than the singlet state at the CCSD(T) and BP86 levels, respectively. The corresponding higher-lying molecular orbitals (MOs) are given in Figure S1. The MO correlation diagram for the singlet state of BP is displayed in Figure S2 that shows a typical 8-valence electronic MO diagram, where four electrons are located in one σ and σ^* orbital, and four electrons are located in two degenerate π orbitals. In the triplet state, one electron from a π-orbital is shifted to a σ-orbital. Qualitatively, both

https://doi.org/10.1021/acs.inorgchem.6c00722
Inorg. Chem. XXXX, XXX, XXX−XXX

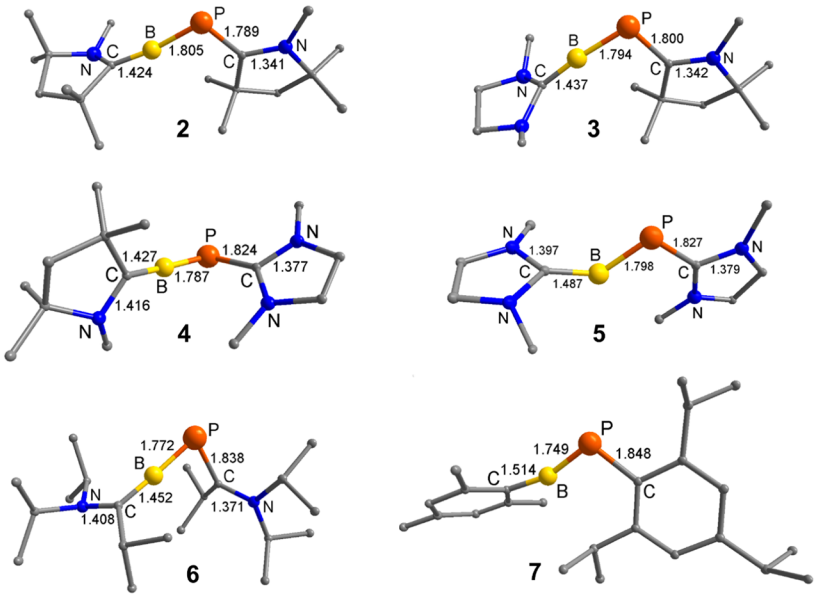

Figure 3. Optimized geometries of **2**−**7** [(L′)B−P(L)] in the singlet ground state [L′, L = cAAC^{Me} (**2**); L′ = NHC^{Me}, L = cAAC^{Me} (**3**); L′ = cAAC^{Me}, L = NHC^{Me} (**4**); L′, L = NHC^{Me} (**5**); L′, L = aAAC (**6**); L′ = Mes, L = Tipp (**7**)] at the BP86-D3(BJ)/def2-TZVP[13a,b,c] level of theory. All bond lengths are given in Å.

singlet and triplet states should have a double bond order as σ and σ^* will cancel each other. But, for polar bonds, bonding and antibonding orbitals do not have exactly equal weightage. Consequently, the WBI values for BP in the singlet and triplet states are found to be 3.14 and 2.20, respectively (see Figure S3). We also performed EDA-NOCV with the triplet BP molecule to check the bonding situation. When several fragmentation schemes are possible, the general prescription to get the most reasonable scheme is to check the size of the orbital interaction (ΔE_{orb}) value. Usually, the smallest value is the best, as it suggests that the charge and electronic states of the chosen fragments are very close to those in the molecule. The numerical values in Table S1 show that B ($2s^2 2p_\sigma^0 2p_\pi^1$) in the doublet state binds with P ($3s^2 3p_\sigma^1 3p_\pi^1 3p_{\pi'}^1$) in the quartet state, forming an electron-sharing π-bond, which is accompanied by one electron B←P dative σ- and π-bonds (see Figure S4 for the deformation densities and the corresponding interacting fragment orbitals). Despite the σ-bond being formed by just one electron, it is even stronger than the combined effect of the two π-bonds. More importantly, SOMO-1 of BP in the triplet state (and LUMO of singlet BP) is appropriate to act as an acceptor orbital for in-phase electron dation from the ligands in the L→BP←L complex (see Figure S2). Therefore, singlet BP should act as a better acceptor than the triplet state, and consequently, we expect that for the ligated monomers, L→BP←L, the singlet state would be more stable than the triplet state, providing better stability and possible synthetic viability in the laboratory compared to the nonligated BP species.

Ligand-Stabilized Monomeric BP Compounds

Next, we investigated the stabilization of the BP moiety by introducing stable singlet carbenes and bulky aromatic ligands to explore the viability of laboratory isolation (Figure 3). Optimizations of compounds **2**−**7** were performed at the BP86-D3(BJ)/def2-TZVP level in both singlet and triplet states. As expected, the singlet state was found to be more stable than the triplet state, with singlet−triplet energy gaps lying in the range of 7.4 to 37.1 kcal/mol (see Tables S2 and S3). All the complexes are energetically stable with respect to the dissociation of two ligands (see Table S4 and related discussion in the SI). NBO analysis was performed on the optimized geometries of **2**−**7** at the BP86-D3(BJ)/def2-TZVP level to investigate the electron density distribution and chemical bonding. Structural variations were introduced by systematically modifying the terminal ligands on the PB framework.

The bonding interactions were further quantified by Mayer bond orders (MBO) and WBI. The C_{cAAC}−P bond in **2** exhibited two natural orbitals: one polarized toward P (62.5%) and another toward C_{cAAC} (37.5%), consistent with partial double bond character (WBI = 1.27; MBO = 1.27). In contrast, the C_{cAAC}−B interaction showed two distinct contributions: a donor−acceptor type interaction, strongly polarized toward carbon (70.6%) and a more delocalized component (59.7% C, 40.1% B). The higher MBO (1.82) value compared to that of WBI (1.51) indicates a bond approaching double bond character. Overall, the B−C_{cAAC} bond exhibited stronger multiple bond character than the P−C_{cAAC} bond, attributable to the greater electron deficiency of B, which enhances π-acceptance. In compound **3**, replacement of the cAAC ligand at B with NHC leads to a single bond occupancy with polarization toward the carbene carbon (69.1%), and corresponding WBI (1.30) and MBO (1.42) values indicative of partial double bond character. For the C_{cAAC}−P bond, a single occupancy is observed with polarization toward C_{cAAC} (65.5%), which is lower than that of the C−B interaction. Unlike compound **2**, the dual σ-donor and π-acceptor interactions observed in the P−C_{cAAC} bonds are absent in compound **3**, reflecting a reduced extent of π-interaction upon ligand substitution. Moving from compounds **2** to **5**, where ligands are changed to NHC on both sides of the PB motif.

In compound **5**, where both termini are substituted with NHC ligands, the C_{NHC}−P bond exhibited a single occupancy with the least MBO (0.99), indicative of a pure single bond

https://doi.org/10.1021/acs.inorgchem.6c00722
Inorg. Chem. XXXX, XXX, XXX−XXX

character and polarization predominantly toward the C_{NHC}. The P−B bond showed polarization toward P (55.8%), indicating an uneven electron density distribution. In contrast, the B−C_{NHC} bond displayed two occupancies: one strongly polarized toward the carbene carbon and the other more polarized toward B, reflecting a combination of donor−acceptor and shared bonding interactions. Among all the compounds analyzed, compound **5** has the least P−C_{NHC} and B−C_{NHC} MBO values and the highest P−B MBO (1.97). The P−B bond exhibited two natural orbitals in compounds **4**, **6**, and **7**, whereas a single occupancy is noted in compounds **2**, **3**, and **5**. It should be noted that the NBO program uses a cutoff value for the occupation to get the 2c−2e (two-centered-two-electron) natural orbitals. So, for any orbital, which has slightly smaller electron occupation than the cutoff value, the program would not categorize them as a 2c−2e natural orbital. However, this does not mean that the double bond character is not there. Nevertheless, the NBO results can at least be used as a first guess about the bonding situation.

The MBO for the P−B interaction increases in the order of **3** < **2** < **6** < **5** < **4** < **7** (1.56 to 1.97), while the WBI follows the trend of **3** < **2** < **5** < **4** < **6** < **7** (1.47 to 1.98). These values are consistent with significant double-bond character, further supported by EDA-NOCV analyses. For the P−C bonds, partial double-bond character is observed, with MBO values increasing in the order of **7** < **5** < **4** < **6** < **3** < **2** (0.99 to 1.27). Similarly, the B−C bonds exhibit partial double-bond character, with MBO values following the trend of **7** < **5** < **3** < **6** < **4** < **2** (1.19 to 1.82). In both cases, the lowest and highest bond orders are consistent; however, these trends are opposite to those observed for the P−B bond. Further NBO analysis revealed that HOMO−2 represents the lone pair on the P atom in general. The HOMO−1 illustrates a π-cloud in compounds **2**−**6**, while in compound **7**, it represents a lone pair on P. The HOMO of all the compounds primarily features the π bond between L′ and B, along with a lone pair on P, except in compound **7**, where it corresponds to the π bond between P and B. The LUMO displays the π^* orbitals of the C═N bond in the P-bonded ligand for compounds **2**−**6**, while in compound **7**, it represents the π bond between the aryl group and B. The natural charge analysis reveals notable variations, as shown in Tables S6, S10 (see SI). For the B atom, a distinct shift is observed with ligand changes: the cAAC-bonded B exhibits a positive charge, whereas the NHC-bonded B displays a negative charge. This indicates that cAAC is a better π-acceptor than NHC, influencing the electronic distribution and stability of the P−B bonds across the series.

The state-of-the-art EDA-NOCV[18] analyses have been performed on compounds **2**−**7** at the BP86-D3(BJ)/TZ2P level to determine the best bonding scenario between B and P atoms (see Tables S25 and S26 in SI). Our studies indicated that the best bonding scenarios[18c] for compounds **2**−**6** involve a dative (D) and electron-sharing (E) interaction between neutral [L-B] and [L-P] in the doublet state, forming an electron-sharing σ-bond and a π dative bond from P to B (Scheme 1).

Compound **7** featured a neutral triplet [L-B] and [L-P] fragments forming an electron-sharing σ and π B−P bond (see Tables S25 and S27). There is also a TippP←BMes σ-backdonation, accounting for 9.6% of the total orbital term, which is significantly less important than the other two bonding contributions of 58.0% and 27.1%, respectively. For **2**−**6**, among the attractive energies, the electrostatic contribution (ΔE_{elstat}) accounts for 40.7−47.4%, while the orbital contribution (ΔE_{orb}) is the most significant, reaching up to 57.1% (see Table S26, Figure 4). The dispersion contribution (ΔE_{disp}) is found to be minimal, ranging from 1.9% to 3.9%. Decomposition of the orbital interactions highlights the dominance of the σ-sharing interaction ($\Delta E_{orb(1)}$), contributing 63.9−73.2% of the total orbital interactions. This reflects the strong covalent interaction between the fragments [LP] and [BL′], driven by the interaction of unpaired electrons residing on the singly occupied orbitals of these fragments. The second orbital contribution ($\Delta E_{orb(2)}$), which accounts for 13.3−18.3% of the total, involves π-backdonation from [LP] to [BL′]. Specifically, in compound **2**, this π-backdonation is characterized by electron donation from the HOMO of [LP] to the LUMO of [BL′], emphasizing the role of π-bonding in stabilizing these systems.

Scheme 1. Possible Bonding Scenarios of Compounds 2−7 [(L′)B−P(L)], Cleaving the B−P Bonds[i]

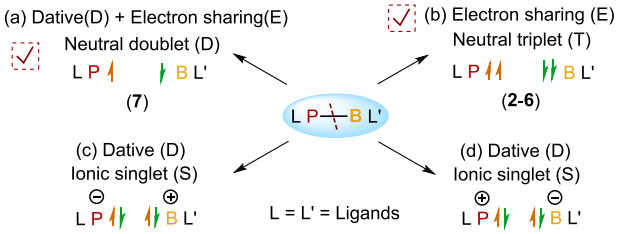

[i][LP] and [BL′] fragments in doublet states (a); in neutral electronic triplet states (b); singly charged $[LP]^-$ and $[BL']^+$ fragments in singlet states (c); and singly charged $[LP]^+$ and $[BL']^-$ fragments in singlet states (d).

To study the bonding between ligands and the central BP moiety, the respective bonds were cleaved, resulting in the fragments [L′L] and [BP]. Our studies revealed the best bonding scenario involving an electron-sharing quintet state, forming two σ-sharing and two π-sharing bonds (see SI). Among the attractive energies, the electrostatic contribution (ΔE_{elstat}) is 36.8−41.8%, and the dispersion energy (ΔE_{disp}) contributes minimally, ranging from 1.6%−2.1%, indicating that van der Waals interactions play a minor role. The orbital interaction energy (ΔE_{orb}), contributing the most at 56.5−61.6%, emphasizes the dominance of covalent bonding in these systems. Decomposing ΔE_{orb} reveals specific contributions from orbital interactions, $\Delta E_{orb(1-4)}$. The σ-electron sharing ($\Delta E_{orb(3)}$ and $\Delta E_{orb(4)}$) accounts for the majority of the orbital interactions, ranging from 54.5% to 61.3%, indicating strong covalent bonds. The π-electron sharing between the fragments ($\Delta E_{orb(1)}$, $\Delta E_{orb(2)}$) contributes 12.3−29.3%, with compound **6** showing the highest π-interaction contribution (29.3%).

Neutral Metallacycles of BP Monomers

Next, we attempted to explore the availability and reactivity of the monomeric boron-phosphides (**2**−**5**) to illustrate the nature of coordination in the presence of group metal(II)-halides (Pd/PtX_2, X = Cl, Br). The optimized geometries of hypothetical nonligated cyclic 3-membered complexes [(BP)-PdX_2] (X = Cl (**8**), Br (**8′**)); [(BP)PtX_2] (X = Cl (**9**), Br (**9′**)); and [((L′)BP(L))(MCl_2)] [L′, L = $cAAC^{Me}$/NHC^{Me}, M = Pd/Pt (**10**-**17**)] at BP86-D3 (BJ)/def2-TZVP are represented in Figure 5, Top. To validate the reliability of the DFT-optimized geometries, single-point CCSD calculations were performed on **8**−**9′**. The corrected energies and T_1

https://doi.org/10.1021/acs.inorgchem.6c00722
Inorg. Chem. XXXX, XXX, XXX−XXX

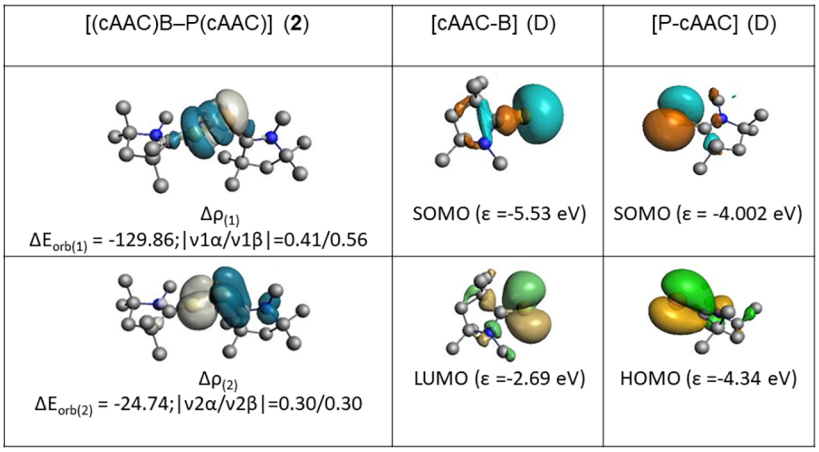

Figure 4. Shapes of the deformation densities $\Delta\rho_{(1)\text{-}(2)}$ that correspond to $\Delta E_{orb(1)\text{-}(2)}$, the associated MOs of (cAAC)B–P(cAAC) (**2**), and the fragment orbitals of [B-cAAC] and [cAAC-P] in the doublet state (D) at the BP86-D3(BJ)/TZ2P[13a,b,c] level. Isosurface values are 0.001 au for $\Delta\rho_{(1-2)}$. The eigenvalues $|\nu_n|$ give the size of the charge migration in e. The direction of the charge flow of the deformation densities is blue→gray. Energies are in kcal/mol.

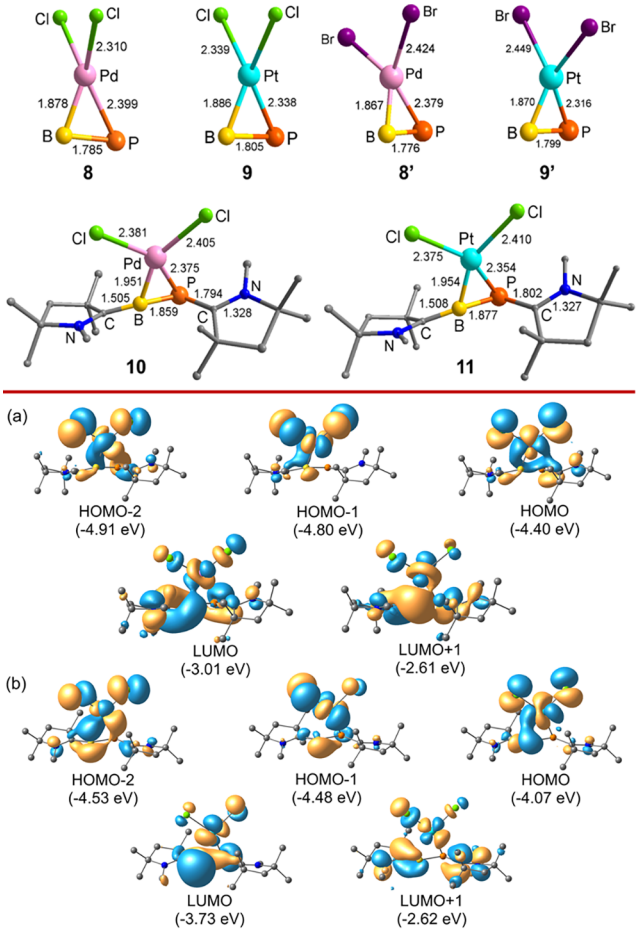

Figure 5. Top: Optimized geometries of **8**–**11** in the singlet ground state, calculated at the BP86-D3(BJ)/def2-TZVP[13] level of theory. All bond lengths are given in Å. See SI for **12**–**17**. Bottom: Selected Kohn–Sham orbitals of **10** (a) and **11** (b), calculated at the BP86-D3(BJ)/def2-TZVP[13] level of theory. See SI for **12**–**17**.

diagnostic values are summarized in Table S11 (see SI). The T_1 diagnostic values for all complexes were found to be below 0.04, which is generally considered acceptable for transition metal complexes, indicating that the single-reference CCSD approach is valid and multireference effects are minimal.[15b] The calculated B–P bond lengths in the above molecules were found to be in the range of 1.776 Å-1.877 Å, which are larger than those of the parent molecules **2**–**5**. NBO analysis revealed two occupancies for the B–P bonds when coordinated with Pd, while it shows one occupancy with Pt. The presence of a 3-centered bond was found in **8**–**9.** The corresponding WBI values (1.50 and 1.37, respectively) suggested that the B–P bond has a partial double bond character in both cases.

We further examined the role of stable singlet carbenes as ligands (cAAC/NHC) for exploring the viability of future laboratory isolation of the predicted 3-membered dihalometallacycles (**10**–**17**). The calculated singlet–triplet energy gaps were found to be highest for complex **11** (16.45 kcal/mol) and lowest for complex **12** (0.58 kcal/mol). The B–P bond lengths in complexes **10**–**17** were found to be in the range of 1.859 Å to 1.895 Å, respectively (see Figure 5), which are significantly larger than that in compound **2** (1.805 Å). The C_{cAAC}–P bond length in complex **13** was found to be slightly longer (1.829 Å) compared to that of other ligated complexes and monomer **2** (1.789 Å). On the other hand, complexes **15** (1.533 Å) and **17** (1.530 Å) showed notable elongation of the C_{cAAC}–B bond lengths compared to that of **2** (1.424 Å). To assess the molecular stability of the ligated metallacycles (**12**–**17**), we calculated the BDE at the M06-L/def2-TZVP (def2-TZVP ECP for the metal) level of theory. The BDE values were found to be significantly higher in all the complexes when the central PBMCl moiety is separated from the ligand, indicating stronger ligand and PBMCl interactions. To study the electronic structure and bonding, NBO analyses were performed at the BP86-D3(BJ)/def2-TZVP level, and the representative Kohn–Sham orbitals are depicted in Figure 5 (see SI for details).

The calculated P–Pd bond order in complex **10** was found to be 0.45, indicating a weak single bond. However, EDA-NOCV analyses provided clearer insight into the electronic structure during bond formation. When $PdCl_2$ is incorporated into compound **2**, it forms a stronger bond with the B atom compared to P. In contrast, platinum chloride establishes bonds with both P and B, leading to the formation of a 3-membered (P–Pt–B) ring in complex **11**. This observation is corroborated by the contour plots of the Laplacian of electron

https://doi.org/10.1021/acs.inorgchem.6c00722
Inorg. Chem. XXXX, XXX, XXX–XXX

density, which reveal no bond path between the P and Pd atoms in complex **10** (see SI). In complexes **10**−**11**, the C_{cAAC}−P bond occupancy decreased from two to one, with respective WBI values of 1.14 and 1.10, respectively, when compared to the monomer **2**. The B−P bond in these complexes exhibited single occupancy, with bond orders of 1.31 (**10**) and 1.01 (**11**). The B−P bond order in compound **2** was found to be 1.48, which is comparable to that of complex **10** (1.31), suggesting the presence of partial double-bond character. However, replacing Pd with Pt reduced the bond order to 1.10 in complex **11**, indicating a transition to single bond character. The B−C_{cAAC} bond, which showed single occupancy in **10**−**11**, contrasts with compound **2**. In both complexes, the B−C_{cAAC} bonds are polarized toward the $C_{carbene}$ center, with bond orders decreasing from 1.51 (**2**) to 0.96 (**10**) and 0.82 (**11**), further confirming the presence of single bond character (Table S17). Significant variations are also observed in the natural charges of the P and B atoms. The natural charges change from 0.013 (P) and 0.215 (B) in **2** to 0.24 (P) and 0.27 (B) in complex **10**, and 0.23 (P) and 0.13 (B) in complex **11**. These changes highlight a notable shift in the electronic environment around the P atom in complexes **10**−**11** compared to that of compound **2**.

To obtain a clear insight into the molecule, we have performed the EDA-NOCV calculation at BP86-D3(BJ)/def2-TZVP level of theory, cleaving the complexes into two fragments, with metal chlorides being one fragment and cAAC-BP-cAAC as the other fragment (Scheme 2). Among these, the most favorable bonding arrangement was found to be the combination of dative and electron-sharing bonds between the fragments $[MCl_2]^-$ and $[cAAC_2BP]^+$. However, in the case of complex **10**, EDA analysis revealed three energy values of ΔE_{orb} that are quite close in proximity (see SI). Two of these correspond to dative and sharing possibilities, mirroring the second bonding scenario, but with two different orbitals of identical energy participating in bond formation while the fragment is in its charged doublet state (Figure 6). The third possibility involved a dative bond between the two fragments in their neutral singlet state. Among the attractive energy components, electrostatic interactions (ΔE_{elstat}) contributed the most, accounting for 62.72% and 62.5% of the total attractive energy in complexes **10** and **11**, respectively. The dispersion interactions (ΔE_{disp}) were found to be relatively small, contributing 4.31% (**10**) and 3.6% (**11**). The ΔE_{orb} accounted for 32.95% of the total attractive interaction in complex **10** and 33.8% in complex **11**, highlighting the significant role of covalent bonding (see Tables S34 and S35). The decomposition of ΔE_{orb} revealed distinct bonding contributions. Within the orbital interactions, π-sharing between the ($cAAC_2BP$) and (MCl_2) fragments emerges as the most significant contributor, with 38.9% in complex **10** and 36% in complex **11**, underscoring the strong π-bonding framework. The π-donation from (MCl_2) to ($cAAC_2BP$) also played a substantial role, contributing 26.3% and 27.4% in complexes **10** and **11**, respectively, indicating effective π-back-donation. The σ-polarization, where electron density is polarized from ($cAAC_2BP$) to (MCl_2), accounts for 12.9% of the total orbital interaction in complex **10** and 13.5% in complex **11**, while σ-donation from (MCl_2) to ($cAAC_2BP$) contributes 4.87% in complex **10** and 8.4% in complex **11**, suggesting stronger σ-donation in the platinum complex. The remaining orbital interactions are relatively minor, at 17.1% (**10**) and 14.6% (**11**) (Figure 6, Tables S33−S35).

Next, we have broken the $[cAAC_2]$−$[PB(MCl_2)]$ bonds to explore four relevant bonding scenarios to understand the interactions between the corresponding fragments (see SI). From our calculations, the best bonding scenario was observed as a combination of dative and electron-sharing bonds (see SI). The ΔE_{orb} accounts for 51.4% of the total attractive interaction in complex **10** and 49.3% in complex **11**, emphasizing the significant role of covalent bonding (Tables S36−S40).

Scheme 2. Possible Bonding Scenarios in 10−11 $[(cAAC)_2BP(MCl_2)]$, Cleaving Bonds between $[MCl_2]$ and $[cAAC_2BP]$ Moieties[i]

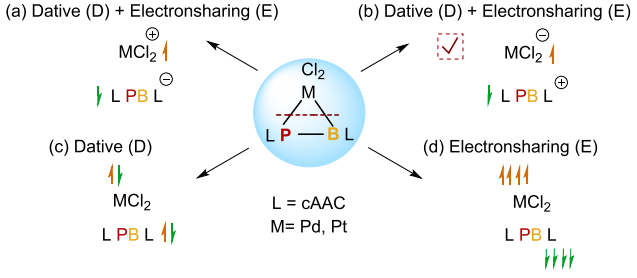

[i]$[cAAC_2BP]$ and $[MCl_2]$ fragments in their singly charged doublet states ((a) and (b)), in neutral singlet states (c), and electron-sharing quintet states (d).

Investigation of Aromaticity for Metallacycles

We have further investigated possible aromaticity in **8**−**17**. The nucleus-independent chemical shift (NICS)[9a] calculations were performed using the GIAO method at different levels of theory for **8**−**11** (Table 1) and **12**−**17** (see SI, Table S48), which revealed significantly negative NICS values at the ring centers and at 1.5 Å above (perpendicular to) the ring plane ($NICS_0$, $NICS_{1.5}$) (see SI). To obtain a more concise and reliable measure of aromaticity, we evaluated the $NICS_{zz}$[9b] values along the molecular and perpendicular planes using Multiwfn (Table 1). To further probe the modulation of aromaticity, the P and B atoms were stabilized through coordination in complexes of the type $[(L')(L)BP(MCl_2)]$ (L′, L = cAAC; M = Pd (**10**), Pt (**11**)). Both complexes **10** and **11** retained aromatic character, as reflected by their negative NICS values, though the extent of aromatic stabilization is weaker than in their corresponding nonligated analogues. Notably, the sites located nearer to the bonds exhibit relatively larger aromaticity values than the NICS(0), consistent with enhanced electron delocalization along the bonding regions. This trend is mainly observed in complexes **10**−**11**, where $NICS_{zz}(0.5)$ is −53.4 ppm, while $NICS_{zz}(0)$ is −36.79 ppm for complex **10**, and $NICS_{zz}(0.5)$ is −74.74 ppm, at the same time $NICS_{zz}(0)$ is −26.45 ppm for complex **11**. In this context, the previously reported metalla-aromatic system, cyclo-PrB_2^- with an NICS value of −22.0 ppm at the ring center,[9b] and RhB_2^- with an NICS value of −88 ppm with Möbius aromaticity are noteworthy.[6] Although the $NICS_{iso}$ values obtained for **8**−**11** in our study are less negative than those reported for RhB_2^-, the corresponding $NICS_{zz}$ values for our systems are significantly larger in magnitude. This observation strongly supports the presence of pronounced π-aromaticity (Figure 7). The osma-pentalene reported by Zhu et al.[19] showed a negative $NICS_{zz}(0)$ value of −11.3 ppm. More recently, Peerless et al.[20] investigated the influence of

https://doi.org/10.1021/acs.inorgchem.6c00722
Inorg. Chem. XXXX, XXX, XXX−XXX

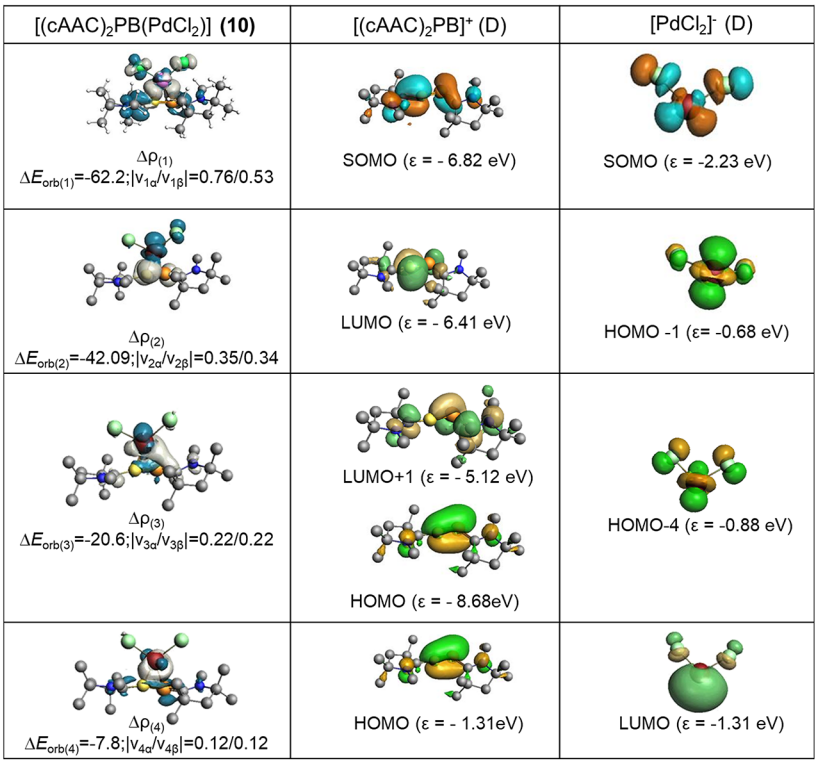

Figure 6. Shapes of the deformation densities $\Delta\rho_{(1)\text{-}(4)}$ that correspond to $\Delta E_{orb(1)\text{-}(4)}$, the associated MOs of $[(cAAC)_2BP(PdCl)_2]$ (**10**), and the fragment orbitals of $[(cAAC)_2BP]$ and $[PdCl_2]$ in its singly charged doublet state (D) at the BP86-D3(BJ)/TZ2P[13] level. Isosurface values are 0.001 au for $\Delta\rho_{(1-4)}$. The eigenvalues $|\nu_n|$ give the size of the charge migration in ε. The direction of the charge flow of the deformation densities is blue→gray. Energies are in kcal/mol.

Table 1. $NICS_{zz}$[9a] Values (In Ppm) for 8−11, Calculated at M06-L/def2-TZVP[13d] (Def2-TZVP ECP[13f] for Metal) Level of Theory along the Perpendicular and Molecular Planes. See SI for 12−17

Complex	8	8′	9	9′	10	11
NICS0$_{(zz)}$	−96.38	−88.93	−95.04	−80.76	−36.79	−26.45
NICS1.5(a)$_{(zz)}$	−13.32	−12.69	−12.90	−11.38	−13.42	−13.09
NICS1.5(b)$_{(zz)}$	−8.31	−7.84	−7.97	−7.50	−11.25	−13.73

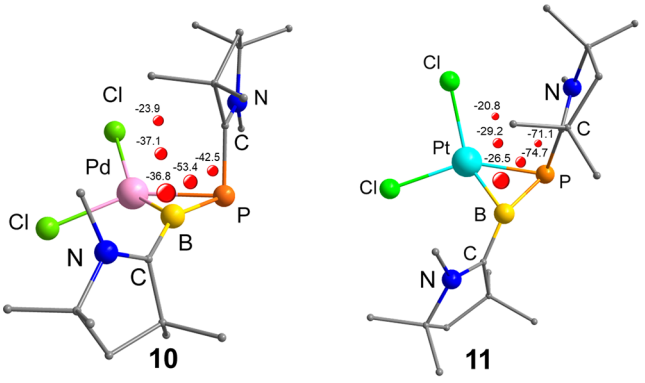

Figure 7. Selected $NICS_{zz}$[9a] values (ppm) for **10**−**11** in both molecular and perpendicular planes with 0.5 Å intervals, calculated at the M06-L/def2-TZVP[13d] (def2-TZVP ECP[13f] form metal) level of theory. See SI for **12**−**17**.

charge on the electronic structure and aromaticity of various Bi_6 clusters.

The consistent negative NICS values indicated aromatic behavior, with the most pronounced aromaticity observed for the dianionic Bi_6^{2-} species, exhibiting a NICS(0) value of −33.4 ppm. Whereas, our system displayed markedly stronger aromatic character, as evidenced by a significantly more negative $NICS_{zz}(0)$ value of −96.38 ppm for **8**.

Next, we performed the GIMIC calculations on complexes **8**−**11** (Figure 8). The current densities, as calculated from the net current strength (see SI, Table S53), are attributed to the structural distortion. Compared to the nonligated species (**8**−**9**), the complexes **10**−**11** approximate a planar structure more closely, which leads to stronger Pd−Cl interactions with delocalized electrons on the Pt/Pd−B−P 3-membered ring, thus weakening the overall ring current density. The previously reported Bi clusters[22] exhibited net ring current densities exceeding +16.2 nAT^{-1}, with the highest value of +31.1 nAT^{-1} observed for the dianionic species Bi_6^{2-}, exhibiting the most negative $NICS_{zz}(0)$ value, indicating a stronger correlation between enhanced ring current density and magnetic aromaticity descriptors. A similar trend is also observed in our systems, where the compound exhibiting the largest current density (+13.81 nAT^{-1}, compound **8**) shows the most negative $NICS_{zz}(0)$ value (−96.38 ppm, compound **8**). Recently, Yadav et al.[22] reported a cationic σ-aromatic Bi_4^{4+} cluster with a comparatively lower ring current density of 9.1 nAT^{-1}.

https://doi.org/10.1021/acs.inorgchem.6c00722
Inorg. Chem. XXXX, XXX, XXX−XXX

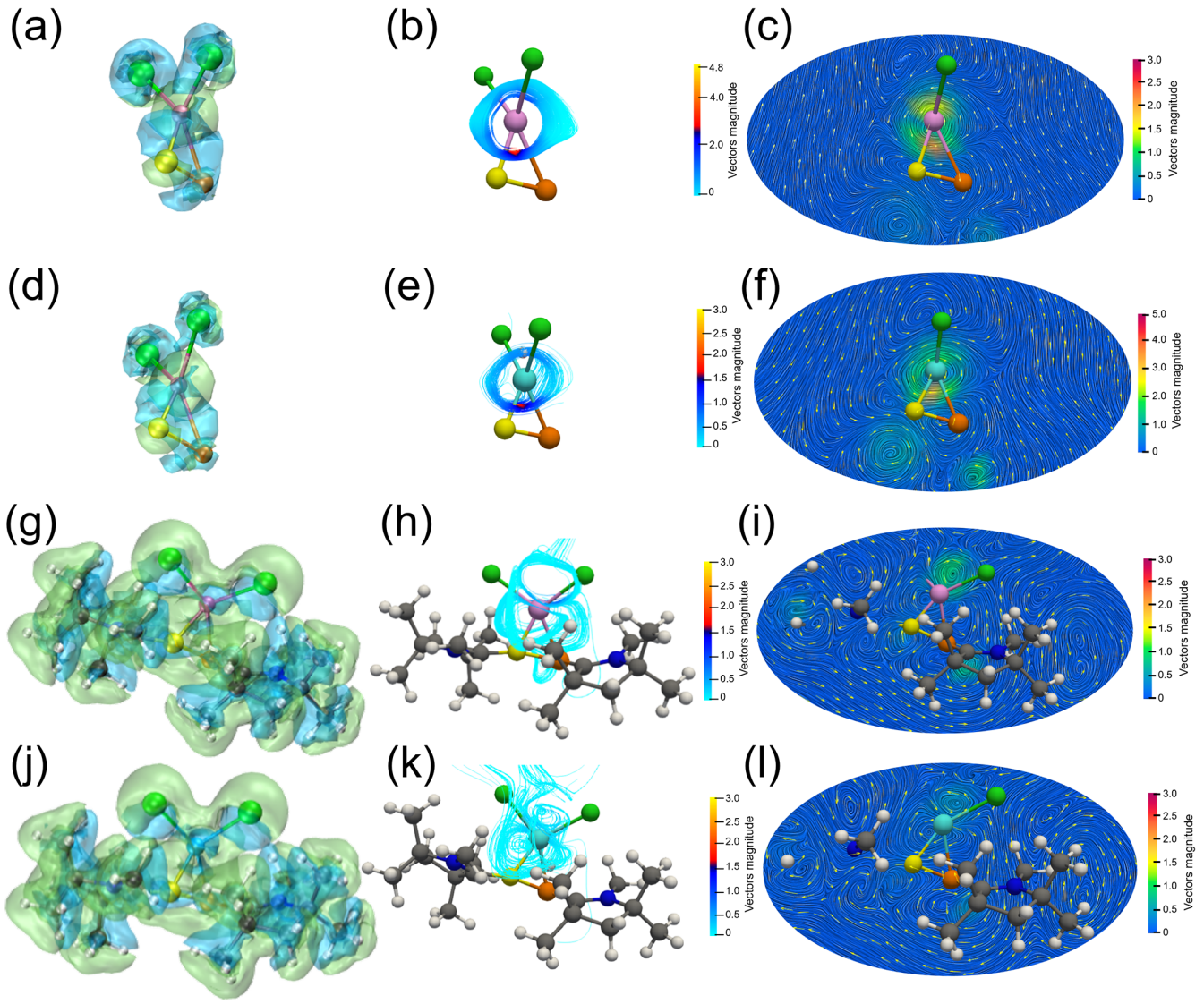

Figure 8. Equivalent surfaces of modes of induced ring currents[17] (diatropic: pale green, paratropic: pale blue) of complexes **8** (a), **9** (d), **10** (g), and **11** (j). Streamline plots of induced current density in **8** (b), **9** (e), **10** (h), and **11** (k). Planar coloring streamline diagrams and arrow diagrams for modes of induced currents in **8** (c), **9** (f), **10** (i), and **11** (l).

In our study, a similar current density value (9.1 nAT^{-1}) is obtained for compound **10**, which represents the least aromatic system among the series and features Pd coordination to the ring. This comparison further supports the consistency between current density values and the degree of aromatic character inferred for our compounds.

The AdNDP analysis was conducted to reveal the intrinsic nature of aromaticity in complexes **8**−**11**. The bonding situation in the three-membered ring is listed in Figure 9.

The phase change Möbius phenomenon in the molecular plane (σ phase) as well as in the perpendicular plane (π phase) was observed in 3c−2e bonds of the complexes **8**−**11** (see Figure 10). As shown in Figure 10, there are three 1c−2e bonds identified as lone pairs on the Pd/Pt atoms, three localized 2c−2e bonds, and three delocalized 3c−2e bonds in complexes **8**−**11**. The occupation numbers of these bonds are above 1.78 |e|, indicating that this series of compounds consists entirely of 16-electron species, which constitutes the 4n electron rules for Möbius aromaticity. However, with respect to the delocalized 3c−2e bonds, differences were observed

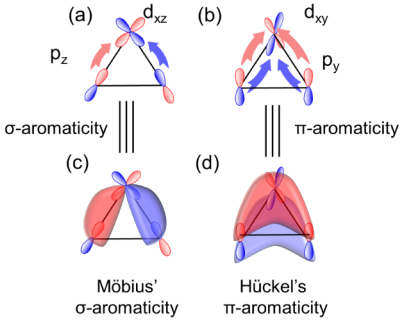

Figure 9. Representation of Hückel and Möbius-type aromaticity in planar three-membered rings. Orbital topology for Möbius σ-aromaticity (a) and (c), and Hückel π-aromaticity (b) and (d).

between the nonligated, and ligated species. In the case of **8**−**9**, there is one 3c−2e σ bond and one 3c−2e π bond, reflecting the double Möbius aromaticity, which was first observed in 3-membered metallacycles, while in the corresponding ligated species (**10**−**11**), both the 3c−2e bonds show σ aromaticity.

https://doi.org/10.1021/acs.inorgchem.6c00722
Inorg. Chem. XXXX, XXX, XXX−XXX

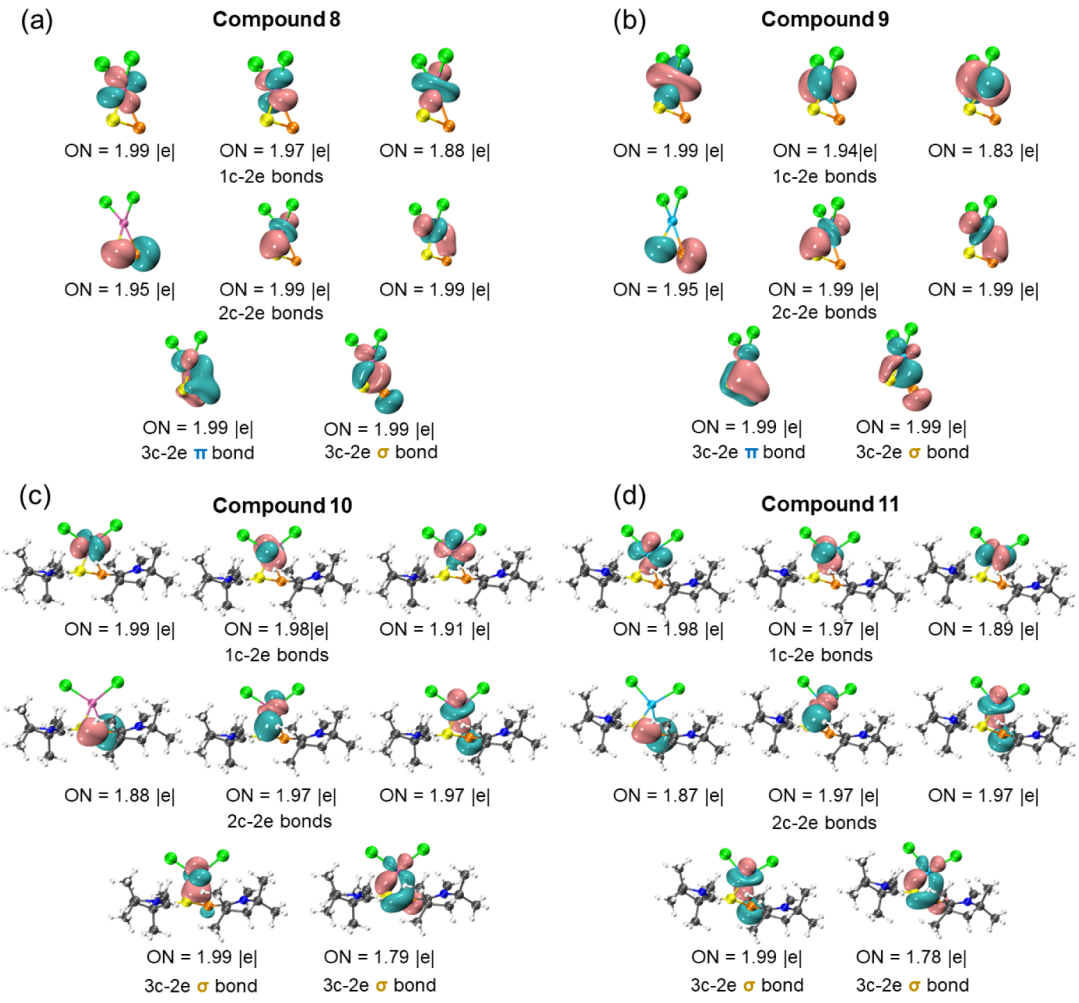

Figure 10. 1c−2e Pd/Pt lone pair, 2c−2e localized bonds, and 3c-2e delocalized bonds in the complexes **8** (a), **9** (b), **10** (c), and **11** (d).

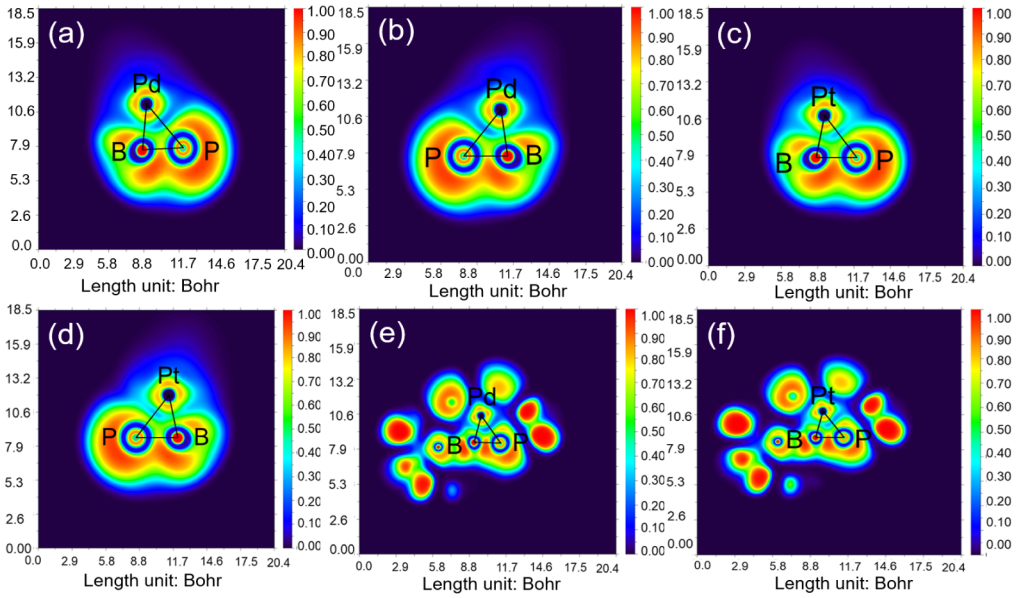

Figure 11. Electron localization function (ELF)[10a−b] plots for **8** (a), **8′** (b), **9** (c), **9′** (d), **10** (e), and **11** (f), at the BP86-D3(BJ)/def2-TZVP[13a,b,c] level of theory. The color bar on the left side indicates increasing localization. The core charge areas are characterized by circular fields around atoms with high (≈1.0) values of ELF (red), while the chemical bonds are described by irregular localization domains (cyan) with smaller values of ELF. See SI for **12**−**17**.

https://doi.org/10.1021/acs.inorgchem.6c00722
Inorg. Chem. XXXX, XXX, XXX−XXX

The aromaticity in **8**−**9** is surprisingly different from that of the previously reported RhB_2^- cluster, which is also a 3-membered ring with 16 electrons, but no double Möbius aromaticity was observed in it. We assume that this is due to the expansion of the ring, resulting from the addition of the P atom and Pt/Pd. The extended bond length inhibited the π coupling among these three atoms, promoting the formation of σ-delocalized bonds and the double Möbius aromaticity. The atomic substitution strategy achieves aromaticity transformation by regulating the size of the 3-membered ring. The disappearance of the double Möbius aromaticity originates from the regulation of the electronic structure of the P and B atoms by ligands.

The presence of ligands enlarged the electron density on P and B, and thus, the P−B distance increased due to the enhanced repulsive forces, which significantly weakened the overlapping π-orbitals of P and B. As a result, 4 electrons were located on one 3c−2e σ bond and one 3c−2e π bond in **8**−**9**, respectively, while 4 electrons were located on the two 3c−2e σ bonds in the ligated complexes **10**−**11**. Thus, AdNDP analysis revealed the presence of three 1c−2e localized bonds (lone pair of Pt/Pd), three types of localized 2c−2e M−P/B (M = Pt, Pd) bonds, and two delocalized 3c−2e bonds in **8**−**10**, which confirmed the Möbius aromaticity with a 16 electron count, following the 4*n* rule. More importantly, the double Möbius aromaticity was first observed in 3-membered metallacycles, and aromaticity transfer was achieved through ligand addition.

Next, we performed the Electron Localization Function (ELF)[10a,b] analyses for complexes **8**−**17** at the BP86-D3(BJ)/def2-TZVP level of theory using Multiwfn[11a,b] software to investigate the distribution of electron pairs (Figure 11, see SI). For complexes **8** and **8′**, two disynaptic basins, *V*(Pd, P) (4.33 *e*) and *V*(Pd, B) (1.75 *e*), and a trisynaptic basin *V*(Pd, P, B) (2.73, 2.78 *e*) were identified, highlighting the dominance of the Pd−P interaction with additional, but weaker, Pd−B participation. Complexes **9** and **9′** exhibited a similar distribution, with two disynaptic basins, *V*(Pt, P) (4.44 *e*), *V*(Pt, B) (2.03 *e*), and a trisynaptic basin *V*(P, B, Pt) (2.63 *e* in **9**, 2.65 *e* in **9′**), indicating that the Pt−P bond constitutes the most localized interaction, supplemented by delocalization across Pt, P, and B atoms (see SI, Figure 11). In contrast, complex **10** displayed one disynaptic basin, *V*(Pd, P) (3.28 *e*) of reduced population relative to complexes **8**−**8′**, together with two trisynaptic basins, *V*(Pd, P, B) (2.33 *e*), and *V*(Pd, C, B) (2.62 *e*), suggesting that multicenter bonding becomes more prominent when a C substituent is present. Complex **11** featured two disynaptic basins, *V*(Pt, P) (3.35 *e*), and *V*(Pt, B) (0.78 *e*), along with three trisynaptic basins, reflecting a further shift toward delocalized multicenter bonding. Overall, these results demonstrate that in complexes **8**−**9′** the M−P bond is the most strongly localized interaction, whereas in complexes **10**−**11**, electron density is more evenly distributed across multicenter basins, indicative of a more delocalized bonding network.[10c]

As demonstrated by Fuentealba and coworkers,[21] pronounced aromatic character was observed for neutral B_6CO_6, and the anionic N_5^- and Al_4^{2-} species, with ELF bifurcation values in the range of 0.7−0.9. To further assess the aromaticity, we analyzed the ELF values at the bifurcation points for both ELF_σ and ELF_π for **8**−**17** (Figure 12, S46) using Multiwfn.[11a,b] Notably, all molecules investigated in our studies exhibited bifurcation values within a comparable range

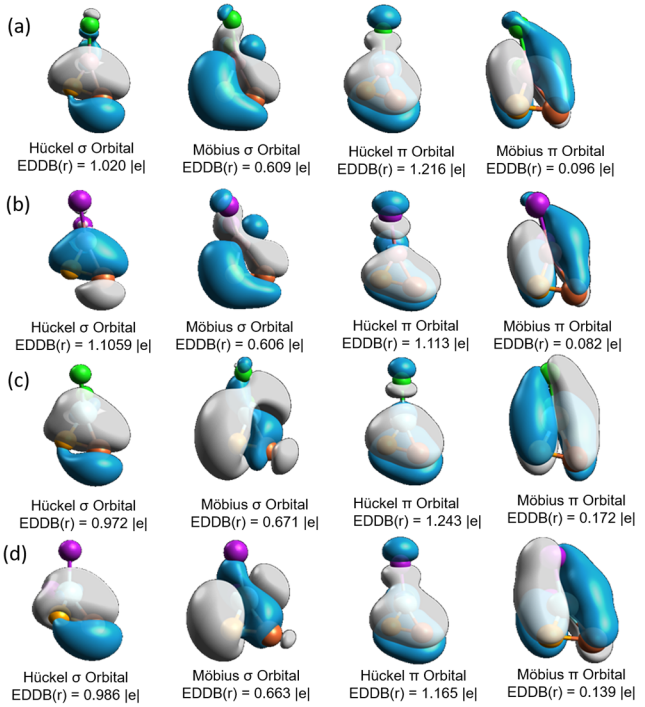

Figure 12. EDDB(r)[12a,b] iso-surfaces and values (|e|) for nonligated complexes **8** (a), **8′** (b), **9** (c), and **9′** (d), and the type of NOBD, calculated at M06-L/def2-TZVP[13d] (def2-TZVP ECP[13f] for metal). See SI for **10**−**17**.

(0.8−0.9), indicating comparable aromatic delocalization. While the highest ELF_π bifurcation value for Al_4^{2-} reaches 0.99, our analysis reveals a closely related ELF_π bifurcation value of 0.92 for complex **14** (see SI, Figure S47), further supporting its pronounced aromatic character. To further assess the aromatic character, ELF values at the bifurcation points for both ELF_σ and ELF_π were analyzed for **8**−**9′** (Figure 12) and **10**−**17** (Figure S46) using Multiwfn software.[11a,b] Across all examined systems, the ELF_π values are found to be in the range of 0.70−0.90, exceeding the commonly accepted aromaticity threshold of 0.70. Such consistently higher ELF_π values strongly support the presence of pronounced aromatic character in the present complexes. For **8**−**9′**, the ELF_σ and ELF_π bifurcation values are observed to be above the threshold range.

For both **8**−**9**, the ELF analysis revealed critical π (0.50) and σ (0.49) type isosurface values, indicating pronounced electron delocalization involving the metal center as well as the P and B atoms. This strong delocalization is fully consistent with the AdNDP results, which identify corresponding 3c−2e π and σ bonding patterns. Upon increasing the ELF isosurface value, bifurcation of the delocalized basins is observed in the peripheral regions, leading to the emergence of localized orbitals at ELF values of 0.7−0.9. At this stage, distinct 2c−2e and 1c−2e bonding features become clearly visible. In parallel, the AdNDP analysis supports this localization trend by yielding well-defined bonding elements with occupation numbers close to 1.99 |e|, confirming the transition from delocalized multicenter bonding to localized bonding interactions. For the ligated compounds **10** and **11**, the ELF isosurfaces prior to bifurcation at approximately 0.5 for the π-type and 0.37−0.43 for the σ-type signify the substantial electron delocalization, analogous to that observed in compounds **8** and **9**. This

https://doi.org/10.1021/acs.inorgchem.6c00722
Inorg. Chem. XXXX, XXX, XXX−XXX

behavior is again corroborated by the AdNDP analysis, which identifies corresponding delocalized bonding orbitals. As bifurcation sets in along the peripheral regions, the ELF basins evolve into localized orbitals that closely mirror the bonding patterns obtained from AdNDP, demonstrating a strong correspondence between the two methodologies. Overall, the combined ELF and AdNDP analysis consistently depicts the balance between delocalized multicenter bonding and localized interactions across the complexes **8**−**11**, highlighting the robustness of the electronic structure description.

Next, we performed the analyses of electron density of delocalized bonds (EDDB) on complexes **8**−**17** to evaluate their aromatic nature and further visualized the molecular orbitals in Avogadro (Figure 12),[12a,b] which revealed that the electron delocalization is dominated by the Hückel channels. The interpretation of the EDDB values is based on the findings of Guha and Sarmah,[12c] who reported similar magnitudes for related systems. Across the series, π-Hückel natural orbital for delocalized bonds (NOBD) contributions (≈1.11−1.24 |e|) are found to be slightly larger than those from σ-Hückel NOBD (≈0.97−1.11 |e|), indicating that the π-framework provides the main source of aromatic stabilization, with σ-delocalization playing a supporting role. The Möbius NOBD contributions are observed to be weaker overall: while the π-Möbius aromaticity was found to be negligible (≈0.08−0.17 |e|), the σ-Möbius pathway remains modest (≈0.61−0.67 |e|), yet smaller than the σ-Hückel aromaticity. Zhu and coworkers reported comparable NOBD values (≈0.8−0.9 |e|) for cyclopropaosmapentalene systems,[23] which were likewise characterized as exhibiting pronounced aromaticity. For the compounds we investigated in our work, the calculated NOBD values are of a similar range, indicating a comparable degree of cyclic electron delocalization. Taken together, our studies revealed the 3-membered Pd/Pt rings as predominantly Hückel π-aromatic systems, with secondary σ-delocalization and minor Möbius character. For the ligated molecules **10**-**17**, the EDDB analysis revealed a different balance of delocalization channels, where the σ-Hückel contributions remain appreciable (0.520 |e| for Pd; 0.551 |e| for Pt) but are now accompanied by significant σ-Möbius delocalization (0.805 |e| for Pd; 0.801 |e| for Pt). Notably, the π-delocalization is essentially quenched upon ligation, leaving the σ-framework as the dominant contributor to the overall aromatic stabilization. This shift indicates that coordination at the metal center not only preserves Hückel-type σ-aromaticity but also promotes additional Möbius σ-delocalization, leading to a mixed aromatic character with a more pronounced σ-component. The EDDB and AdNDP results were found to be fully consistent, which likewise showed the disappearance of π-delocalization and the emergence of σ-dominated aromaticity upon ligation of the predicted 3-membered metallacycles.

CONCLUSION

In conclusion, we have investigated the chemical bonding and reactivity of molecular boron-phosphides, stabilized by electronically tuned homo- and heterobileptic donor-base ligands via their incorporation into the 3-membered dihalometallacycles by quantum chemical methods. Remarkably, our studies unraveled the unique Hückel and Möbius types of profound σ aromaticity in the unprecedented neutral planar 3-membered p-block-based heteronuclear metallacycles [(L′)-(L)BP(MCl_2)] (**10**−**17**) in the presence of stable singlet carbenes as the ligands, even though the corresponding non-ligated complexes [(BP)MCl_2] (**8**−**9**) exhibited both σ and π aromaticity, as confirmed by the detailed NICS, ELF, AdNDP, and EDDB calculations. Our strategy opens up an efficient way to modulate the electronic structures and thereby paves the path for designing novel boron-phosphide-based heteroaromatic metallacycles.

ASSOCIATED CONTENT

Supporting Information

The Supporting Information is available free of charge at https://pubs.acs.org/doi/10.1021/acs.inorgchem.6c00722.

Cartesian coordinates (XYZ)

Additional computational details and methods, including representative figures, tables, and schemes. (DOC/XYZ/PDF) (PDF)

AUTHOR INFORMATION

Corresponding Authors

Sudipta Roy − *Department of Chemistry, Indian Institute of Science Education and Research (IISER) Tirupati, Tirupati 517619 Andhra Pradesh, India;* orcid.org/0000-0002-5883-4329; Email: roy.sudipta@iisertirupati.ac.in

Di Sun − *School of Chemistry and Chemical Engineering, Shandong University, Ji'nan 250100, People's Republic of China;* orcid.org/0000-0001-5966-1207; Email: dsun@sdu.edu.cn

Sudip Pan − *Centre for Interdisciplinary Research (CIDR), SRM University − AP, Amaravati 522502 Andhra Pradesh, India;* orcid.org/0000-0003-3172-926X; Email: sudip.p@srmap.edu.in

Authors

Akshara Purushothaman − *Department of Chemistry, Indian Institute of Science Education and Research (IISER) Tirupati, Tirupati 517619 Andhra Pradesh, India*

Hao Liang − *School of Chemistry and Chemical Engineering, Shandong University, Ji'nan 250100, People's Republic of China*

Farsana Abdul Salam − *Department of Chemistry, Indian Institute of Science Education and Research (IISER) Tirupati, Tirupati 517619 Andhra Pradesh, India;* orcid.org/0009-0003-2267-3847

Antarik Parashar − *Department of Chemistry, Indian Institute of Technology Madras, Chennai 600036 Tamil Nadu, India*

Maria Francis − *Department of Chemistry, Indian Institute of Science Education and Research (IISER) Tirupati, Tirupati 517619 Andhra Pradesh, India;* orcid.org/0000-0002-0506-4885

Complete contact information is available at: https://pubs.acs.org/10.1021/acs.inorgchem.6c00722

Author Contributions

#A.P. and H.L. contributed equally.

Notes

The authors declare no competing financial interest.

ACKNOWLEDGMENTS

This work was financially supported by ANRF-SERB, New Delhi, for the POWER grant (SPG/2021/003237), STARS-IISC, MoE, Govt. of India (MoE-STARS/STARS-2/2023-

0666), IISER Tirupati to S.R., and the National Natural Science Foundation of China (Grant Nos. 92361301, 22171164, 22325105, 52261135637) to D.S. S.P. thanks SRM University - AP for the Seed grant. Prof. Di Sun would like to thank Prof. Sukhendu Mandalin Indian Institute of Science Education and Research Thiruvananthapuram for some interesting discussions.

REFERENCES

(1) Gan, Z.; Grant, D. J.; Harrison, R. J.; Dixon, D. A. The Lowest Energy States of the Group-IIIA−Group-va Heteronuclear Diatomics: BN, BP, AlN, and AlP from Full Configuration Interaction Calculations. *J. Chem. Phys.* **2006**, *125*, 124311.

(2) Yang, W.; Krantz, K. E.; Dickie, D. A.; Molino, A.; Wilson, D. J. D.; Gilliard, R. J., Jr. Crystalline BP-Doped Phenanthryne via Photolysis of The Elusive Boraphosphaketene. *Angew. Chem., Int. Ed.* **2020**, *59* (10), 3971−3975.

(3) Li, X.; Kuznetsov, A. E.; Zhang, H.; Boldyrev, A. I.; Wang, L. Observation of All-Metal Aromatic Molecules. *Science* **2001**, *291*, 859−861.

(4) Tsipis, A. C.; Tsipis, C. A. Ligand-Stabilized Aromatic Three-Membered Gold Rings and Their Sandwichlike Complexes. *J. Am. Chem. Soc.* **2005**, *127* (30), 10623−10638.

(5) Blanchard, S.; Fensterbank, L.; Gontard, G.; Lacôte, E.; Maestri, G.; Malacria, M. Synthesis of Triangular Tripalladium Cations as Noble-Metal Analogues of the Cyclopropenyl Cation. *Angew. Chem., Int. Ed.* **2014**, *53* (7), 1987−1991.

(6) Wang, Z.-L.; Chen, T.-T.; Chen, W.-J.; Li, W.-L.; Zhao, J.; Jiang, X.-L.; Li, J.; Wang, L.-S.; Hu, H.-S. The Smallest 4f-Metalla-Aromatic Molecule of Cyclo-PrB_2^- with Pr−B Multiple Bonds. *Chem. Sci.* **2022**, *13* (34), 10082−10094.

(7) Braunschweig, H.; Damme, A.; Dewhurst, R. D.; Vargas, A. Bond-strengthening π backdonation in a transition-metal π-diborene complex. *Nat. Chem.* **2013**, *5* (2), 115−121.

(8) (a) Braunschweig, H.; Dewhurst, R. D.; Gessner, V. H. Transition Metal Borylene Complexes. *Chem. Soc. Rev.* **2013**, *42* (8), 3197−3208. (b) Legare, M.-A.; Pranckevicius, C.; Braunschweig, H. Metallomimetic Chemistry of Boron. *Chem. Rev.* **2013**, *5* (2), 8231−8261.

(9) (a) Chen, Z.; Wannere, C. S.; Corminboeuf, C.; Puchta, R.; Schleyer, P. V. R. Nucleus-independent chemical shifts (NICS) as an aromaticity criterion. *Chem. Rev.* **2005**, *105* (10), 3842−3888. (b) Gershoni-Poranne, R.; Stanger, A. The NICS-*XY*-Scan: Identification of Local and Global Ring Currents in Multi-Ring Systems. *Chem. − Eur. J.* **2014**, *20* (19), 5673−5688.

(10) (a) Tian, L.; Fei-Wu, C. Wuli Huaxue Xuebao. Meaning and Functional Form of the Electron Localization Function. *Acta Phys. -Chim. Sin.* **2011**, *27* (12), 2786−2792. (b) Fuentealba, P.; Chamorro, E.; Santos, J. C. Chapter 5 Understanding and Using the Electron Localization Function. *Theor. Comput. Chem.* **2007**, *19*, 57−85. (c) Cui, L.-J.; Liu, Y.-Q.; Pan, S.; Cui, Z.-H.; Frenking, G. Unusual Quadruple Bonds Featuring Collective Interaction-Type σ Bonds between First Octal-Row Atoms in the Alkaline-Earth Compounds $AeOLi_2$ (Ae = Be−Ba). *Chem. Sci.* **2024**, *15* (36), 14705−14720.

(11) (a) Lu, T.; Chen, F. Multiwfn: A Multifunctional Wavefunction Analyzer. *J. Comput. Chem.* **2012**, *33* (5), 580−592. (b) Lu, T. A Comprehensive Electron Wavefunction Analysis Toolbox for Chemists, Multiwfn. *J. Chem. Phys.* **2024**, *161* (8), 082503.

(12) (a) Szczepanik, D. W. *EDDBRunScript*; https://aromaticity.uj.edu.pl/software/#runeddb. (accessed 11 August 2025). (b) Hanwell, M. D.; Curtis, D. E.; Lonie, D. C.; Vandermeersch, T.; Zurek, E.; Hutchison, G. R. Avogadro: An Advanced Semantic Chemical Editor, Visualization, and Analysis Platform. *J. Cheminf.* **2012**, *4*, 17. (c) Sarmah, K.; Guha, A. K. Quest for Double Möbius Aromaticity. *Chem. − Eur. J.* **2024**, *30* (28), No. e202400395.

(13) (a) Becke, A. D. Density-Functional Exchange-Energy Approximation with Correct Asymptotic Behavior. *Phys. Rev. A* **1988**, *38* (6), 3098−3100. (b) Perdew, J. P. Density-Functional Approximation for the Correlation Energy of the Inhomogeneous Electron Gas. *Phys. Rev. B* **1986**, *33* (12), 8822−8824. (c) Weigend, F.; Ahlrichs, R. Balanced Basis Sets of Split Valence, Triple Zeta Valence and Quadruple Zeta Valence Quality for H to Rn: Design and Assessment of Accuracy. *Phys. Chem. Chem. Phys.* **2005**, *7* (18), 3297. (d) Zhao, Y.; Truhlar, D. G. The M06 Suite of Density Functionals for Main Group Thermochemistry, Thermochemical Kinetics, Noncovalent Interactions, Excited States, and Transition Elements: Two New Functionals and Systematic Testing of Four M06-Class Functionals and 12 Other Functionals. *Theor. Chem. Acc.* **2008**, *120* (1−3), 215−241. (e) Adamo, C.; Barone, V. Toward Reliable Density Functional Methods without Adjustable Parameters: The PBE0Model. *J. Chem. Phys.* **1999**, *110* (13), 6158−6170. (f) Minnette, W. E.; Hoy, E. P.; Sand, A. M. The Use of Effective Core Potentials with Multiconfiguration Pair-Density Functional Theory. *J. Phys. Chem. A* **2024**, *128* (31), 6555−6565.

(14) Frisch, M. J.; Trucks, G. W.; Schlegel, H. B.; Scuseria, G. E.; Robb, M. A.; Cheeseman, J. R.; Scalmani, G.; Barone, V.; Petersson, G. A.; Nakatsuji, H., et al. *Gaussian 09 Revision D.01*; Gaussian, Inc.: Wallingford, CT, 2016.

(15) (a) Purvis, G. D.; Bartlett, R. J. A Full Coupled-Cluster Singles and Doubles Model: The Inclusion of Disconnected Triples. *J. Chem. Phys.* **1982**, *76* (4), 1910−1918. (b) Kalita, A. J.; Rohman, S. S.; Kashyap, C.; Ullah, S. S.; Guha, A. K. Transition Metal Carbon Quadruple Bond: Viability through Single Electron Transmutation. *Phys. Chem. Chem. Phys.* **2020**, *22* (42), 24178−24180.

(16) (a) Reed, A. E.; Curtiss, L. A.; Weinhold, F. Intermolecular Interactions from a Natural Bond Orbital, Donor-Acceptor Viewpoint. *Chem. Rev.* **1988**, *88* (6), 899−926. (b) Glendening, E. D.; Landis, C. R.; Weinhold, F. NBO 6.0: Natural Bond Orbital Analysis Program. *J. Comput. Chem.* **2013**, *34* (16), 1429−1437.

(17) Jusélius, J.; Sundholm, D.; Gauss, J. Calculation of Current Densities Using Gauge-Including Atomic Orbitals. *J. Chem. Phys.* **2004**, *121* (9), 3952−3963.

(18) (a) Mitoraj, M.; Michalak, A. Applications of Natural Orbitals for Chemical Valence in a Description of Bonding in Conjugated Molecules. *J. Mol. Model.* **2008**, *14* (8), 681−687. (b) Mitoraj, M. P.; Michalak, A. σ-Donor and π-Acceptor Properties of Phosphorus Ligands: An Insight from the Natural Orbitals for Chemical Valence. *Inorg. Chem.* **2010**, *49* (2), 578−582. (c) Zhao, L.; Pan, S.; Holzmann, N.; Schwerdtfeger, P.; Frenking, G. Chemical Bonding and Bonding Models of Main Group Compounds. *Chem. Rev.* **2019**, *119* (14), 8781−8845.

(19) Zhu, C.; Luo, M.; Zhu, Q.; Zhu, J.; Schleyer, P. V. R.; Wu, J. I.-C.; Lu, X.; Xia, H. Planar Möbius Aromatic Pentalenes Incorporating 16 and 18 Valence Electron Osmiums. *Nat. Commun.* **2014**, *5* (1), 3265.

(20) Peerless, B.; Schmidt, A.; Franzke, Y. J.; et al. φ-Aromaticity in prismatic $\{Bi_6\}$-based clusters. *Nat. Chem.* **2023**, *15*, 347−356.

(21) Santos, J. C.; Tiznado, W.; Contreras, R.; Fuentealba, P. *Sigma−Pi* Separation of the Electron Localization Function and Aromaticity. *J. Chem. Phys.* **2004**, *120* (4), 1670−1673.

(22) Yadav, R.; Maiti, A.; Schorpp, M.; et al. Supramolecular trapping of a cationic all-metal σ-aromatic $\{Bi_4\}$ ring. *Nat. Chem.* **2024**, *16*, 1523−1530.

(23) Pan, S.; Yan, J.; Li, W.; Shuai, Z.; Zhu, J. Too Persistent to Resist: Aromaticity in 16e Osmapentalene Radicals Survives regardless of Redox. *Chemistry* **2025**, *7* (1), 22−22.

https://doi.org/10.1021/acs.inorgchem.6c00722
Inorg. Chem. XXXX, XXX, XXX−XXX